


Structures of wild-type and selected CMT1X mutant connexin 32 gap junction channels and hemichannels

Journal Article

Author(s):

Qi, Chao; Lavriha, Pia; Bayraktar, Erva; Vaithia, Anand; [Schuster, Dina](#) ; Pannella, Micaela; Sala, Valentina; Picotti, Paola; Bortolozzi, Mario; Korkhov, Volodymyr M.

Publication date:

2023-09

Permanent link:

<https://doi.org/10.3929/ethz-b-000630228>

Rights / license:

[Creative Commons Attribution-NonCommercial 4.0 International](#)

Originally published in:

Science Advances 9(35), <https://doi.org/10.1126/sciadv.adh4890>

Funding acknowledgement:

184951 - Structure and function of the adenylyl cyclase-containing signal transduction complexes (SNF)



STRUCTURAL BIOLOGY

Structures of wild-type and selected CMT1X mutant connexin 32 gap junction channels and hemichannels

Chao Qi^{1,2†}, Pia Lavriha^{1,2†}, Erva Bayraktar^{3,4†}, Anand Vaithia^{1,2}, Dina Schuster^{1,2,5}, Micaela Pannella^{3,4}, Valentina Sala³, Paola Picotti⁵, Mario Bortolozzi^{3,4*}, Volodymyr M. Korkhov^{1,2*}

In myelinating Schwann cells, connection between myelin layers is mediated by gap junction channels (GJs) formed by docked connexin 32 (Cx32) hemichannels (HCs). Mutations in Cx32 cause the X-linked Charcot-Marie-Tooth disease (CMT1X), a degenerative neuropathy without a cure. A molecular link between Cx32 dysfunction and CMT1X pathogenesis is still missing. Here, we describe the high-resolution cryo-electron cryo-myography (cryo-EM) structures of the Cx32 GJC and HC, along with two CMT1X-linked mutants, W3S and R22G. While the structures of wild-type and mutant GJs are virtually identical, the HCs show a major difference: In the W3S and R22G mutant HCs, the amino-terminal gating helix partially occludes the pore, consistent with a diminished HC activity. Our results suggest that HC dysfunction may be involved in the pathogenesis of CMT1X.

INTRODUCTION

Connexin-mediated communication is one of the major pathways of intercellular signaling (1, 2), involving complex physiological and pathological processes, such as electrical activity of the heart (3), neuronal signaling (4), release of hormones (5), immunity (6), inflammation (7), cancer (8), and cell death (9). The importance of connexin-mediated communication is underscored by at least 28 genetic diseases linked to mutations in the 21 genes encoding connexins in humans (10–11).

Connexin isoforms share a conserved molecular architecture: Each is a four-transmembrane (TM) domain protein that assembles into hexamers called connexons or hemichannels (HCs). Two HCs expressed at juxtaposed plasma membrane regions of adjacent cells, or even the same cell, can dock together to form a gap junction (GJ) channel (GJC) (11). Tens to thousands of GJs assemble in a regular hexagonal pattern (a GJ plaque), which allows direct intercellular exchange of ions, metabolites, second messengers [e.g., cyclic adenosine 3',5'-monophosphate (cAMP) and inositol 1,4,5-trisphosphate (IP₃)], or peptides (12). Unlike GJs, connexin HCs are normally closed at rest but can open under physiological conditions, allowing sustained ion fluxes and release of adenosine 5'-triphosphate (ATP), nicotinamide adenine dinucleotide (oxidized form) (NAD⁺), glutamate, and other signaling molecules into the extracellular space (13).

Connexin 32 (Cx32) protein, encoded by the *GJB1* gene, is not only strongly expressed in the liver (14) but also found in various tissues throughout the body, including the central and peripheral nervous systems (15, 16). In the peripheral nervous system, Cx32 is expressed in myelinating Schwann cells, particularly in noncompact regions of the myelin sheath (15, 17), where GJs were

proposed to provide a radial diffusion pathway between the abaxonal and adaxonal regions (Fig. 1A) (18). Moreover, extracellular release of ATP by Cx32 HCs has been proposed to support purinergic signaling triggered by neuronal activity, thus regulating Schwann cell myelin maintenance (19, 20).

Mutations of Cx32 that affect its biosynthesis, folding, assembly, trafficking, or channel properties are the leading cause of the X-linked form of Charcot-Marie-Tooth disease (CMT1X), a dominant neuromuscular degenerative disorder (21–23). Axonal and myelin defects in peripheral neurons of CMT1X patients lead to progressive sensory abnormalities and muscle atrophy. The disease clinical onset usually occurs in the first two decades of a patient's life and no cure is available (20, 24). Loss of function of GJs and/or HCs due to Cx32 mutations is presumed to be the prevailing cause of the disease [reviewed in detail in (20)], although the molecular and cellular mechanisms underlying its pathogenesis remain unclear.

Despite the importance of Cx32 in human physiology and pathology, the structure of this protein has not yet been described. Insights into the structure-function relationships of Cx32 have been derived indirectly through homology modeling from the structures of other connexin proteins (25–27).

To date, the structures of four connexin complexes have been experimentally determined: Cx26 GJC (28–31), Cx46/50 GJC (32, 33), Cx31.3 HC (34), Cx36 GJC (35), and Cx43 GJC and HC (36, 37). These homologous structures have not only provided important clues to the shared architectural features and assembly of connexin-mediated GJs and HCs but also revealed substantial differences between them. To advance our understanding of the molecular basis of Cx32 channel activity and regulation in health and disease, we used electron cryo-microscopy (cryo-EM) to determine the structures of the HCs and GJs formed by Cx32 wild-type (WT) as well as the two mutants, W3S and R22G, linked to CMT1X.

RESULTS

Structures of the Cx32 GJC and HC

The Cx32 protein tagged with a C-terminal yellow fluorescent protein (YFP) was chosen for large-scale protein expression for

¹Institute of Molecular Biology and Biophysics, ETH Zurich, Zurich, Switzerland.

²Laboratory of Biomolecular Research, Paul Scherrer Institute, Villigen, Switzerland.

³Veneto Institute of Molecular Medicine (VIMM), Padua, Italy. ⁴Department of

Physics and Astronomy "G. Galilei", University of Padua, Padua, Italy. ⁵Institute of Molecular Systems Biology, ETH Zurich, Zurich, Switzerland.

*Corresponding author. Email: volodymyr.korkhov@psi.ch (V.M.K.); mario.bortolozzi@unipd.it (M.B.)

†These authors contributed equally to this work.

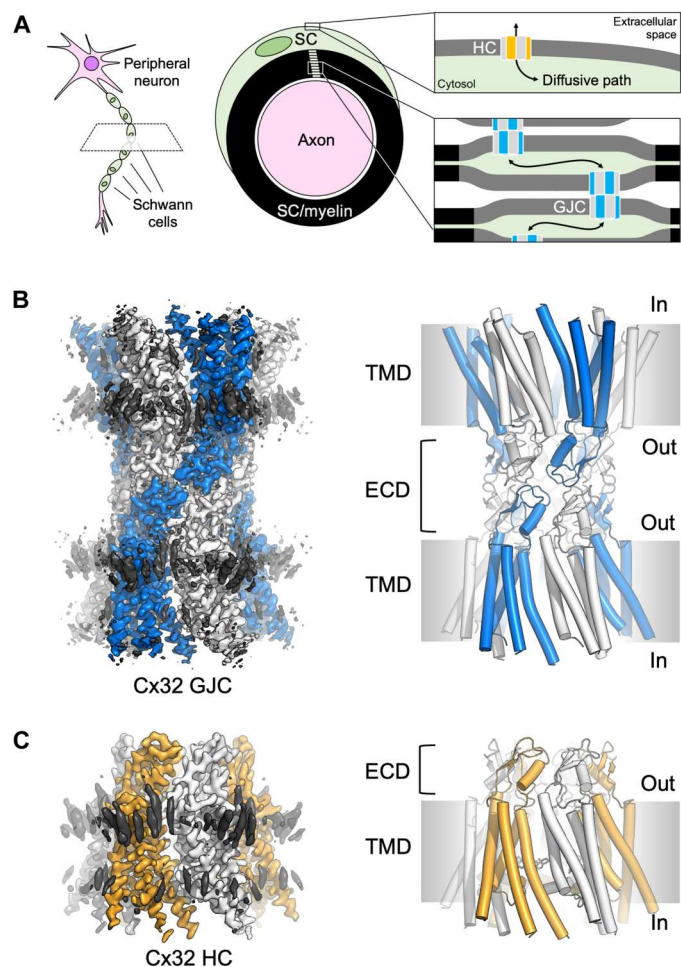


Fig. 1. Cryo-EM structures of Cx32 GJC and HC. (A) Illustration of Cx32 GJCs and HCs in distinct membrane compartments of the myelinating Schwann cells (SC). (B) Cryo-EM map and model of Cx32 GJC. Cx32 is surrounded by lipid-like molecules at the outer leaflet and inner leaflet of the membrane (black density). (C) Cryo-EM map and model of Cx32 HC.

structural studies. To ascertain that this construct can be used to generate active GJCs, we used the dual patch-clamp technique to measure the GJ conductance (g_j) in HeLa DH cells (fig. S1). The measured g_j values confirmed the expression of functional Cx32 GJCs, whereas control cells exhibited negligible intercellular communication. Both Cx32 GJCs (g_j values) and HCs (g_m values) were sensitive to cytoplasm acidification mediated by extracellular CO_2 , consistent with our previous study (27).

Cx32-YFP construct was expressed in human embryonic kidney (HEK) 293F cells, and the protein preparations were purified using anti-green fluorescent protein (GFP) nanobody affinity chromatography, followed by size exclusion chromatography (fig. S2A). The protein samples with the affinity tag removed were concentrated, vitrified on cryo-EM grids, and used for cryo-EM analysis (figs. S3 and S6A). The sample featured very well preserved full GJC structures, evident particularly in the thin ice areas of the cryo-EM grids (fig. S3). We determined the cryo-EM reconstruction of the Cx32 GJC in D6 symmetry, at 2.14-Å resolution, revealing the fine details of the protein structure (Fig. 1, B and C, and figs. S3C

and S8A). The quality of the resulting density map revealed alternative side-chain conformations, ordered water molecules (fig. S8, A and C), and a number of lipid- or detergent-like density elements at the protein-lipid domain boundary (Fig. 1B). Furthermore, using the same micrographs and focusing on processing of the smaller HC particles, we were able to reconstruct the structure of the Cx32 HC at a 3.06-Å resolution in C6 symmetry (Fig. 1C and figs. S3C and S6B). Processing of the cryo-EM data in C1 symmetry confirmed the presence of all density map features observed with C6 or D6 symmetry imposed for HC and GJC, respectively (figs. S3C and S7, A and B, and table S1).

Comparison of Cx32 GJC and HC structures

The overall conformation of the Cx32 HC appears to be very similar to the connexon of a fully assembled GJC (Fig. 2, A to D, and fig. S10A). There are two key differences that concern the extracellular loops (ECL1 and ECL2) and the N-terminal helix (NTH) regions of Cx32.

ECL1 and ECL2 of the Cx32 GJC connexon show a slight conformational rearrangement, compared to those in the HC (fig. S10, A and B). This conformational rearrangement is very similar to that of Cx43 we observed previously (37). Cx32 belongs to the β group connexins based on the inter-HC interface. It shares the same interface residues with Cx26 (N54-N57 in ECL1 and N175-D178 in ECL2; fig. S10C). As a consequence of this similarity in sequence and structure, Cx32 is capable of forming heterotypic GJCs with Cx26. In contrast, the α group of connexins, which includes Cx43, is not compatible with the β group. Nevertheless, Cx32 and Cx43 use a similar mechanism to assemble a GJC, whereby ECL1 and ECL2 move outward to dock the two HCs and form a full GJC.

The NTH of Cx32 is a fundamentally important domain that regulates both permeability and gating of GJCs and HCs. It regulates the voltage- (V_j -) gating polarity, the current-voltage (I - V) relation, and the single-channel conductance (38–40). Furthermore, previous findings related to other CMT1X mutations in the NTH and the TM1 of Cx32 found that these domains are implicated in GJ formation, thus affecting cell-cell junctional coupling (41–43). The NTH of the Cx32 HC is very well ordered and adopts a previously undescribed conformation (Fig. 2, C and D), unlike the NTH of the GJC that appears to be poorly ordered. We did not build the NTH in our Cx32 GJC model due to the poor quality of the GJC density map in the corresponding region; only approximate placement of the NTH is possible (Fig. 2, A and B). On the basis of the mass spectrometry (MS) analysis, the Met¹ residue is present in our Cx32 sample, which is different from Cx31.3 (34) and Cx43 (fig. S11) (37), and therefore, our model of the Cx32 HC includes Met¹. The NTH of Cx32 HC is positioned parallel to the membrane plane, maintaining an open pore conformation (Fig. 2, C and D). Although the structures of both the GJC and the HC represent an open pore state, the rigid conformation of the NTH in the Cx32 HC constricts the pore to a diameter of ~ 11 Å at the cytosolic side (Fig. 2B). In contrast, the pore diameter in the GJC, based on the ordered region of the protein, is ~ 15 Å (fig. S12C), not accounting for the present flexible NTH regions. The lack of clearly defined NTH conformations in the GJC suggests that the two connexons are fully open and may allow free unselective movement of both anions and cations (44), as well as small molecules. The arrangement of the NTH in the HC not only reduces the size of the pore but also markedly remodels the charge distribution at the cytosolic

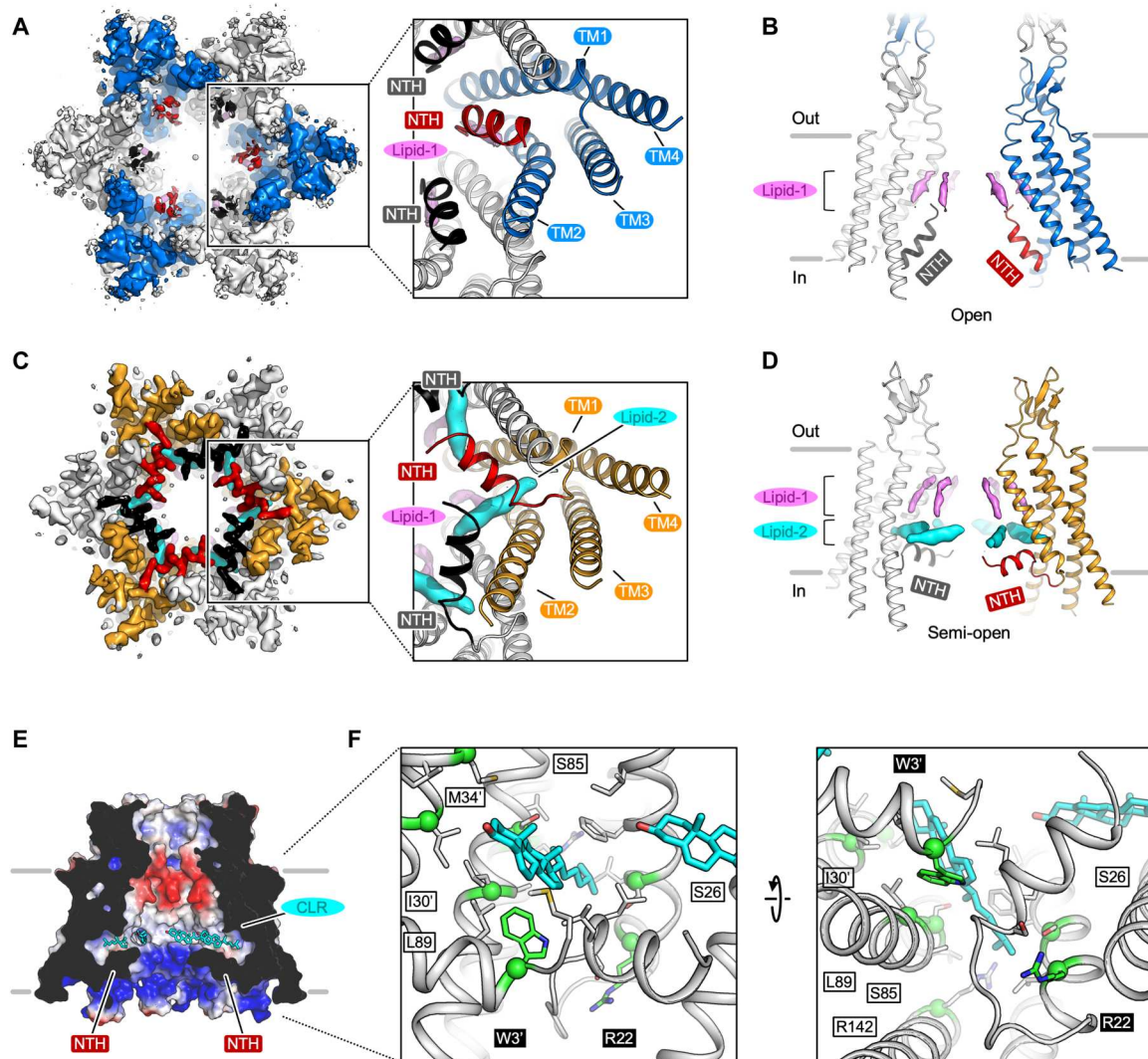


Fig. 2. Comparisons of Cx32 GJC and HC. (A and B) Cryo-EM map (bottom view) and model (side view) of Cx32 GJC. The NTH (red and black) inserts to the channel pore, representing the open state of GJC. The lipid-1 density is labeled using pink color. (C and D) Cx32 HC map (bottom view) and model (side view). The NTH (red and black) is parallel to the membrane layer, shrinking the pore of Cx32 HC to about 11 Å. Lipid-2 (cyan) is stabilized by NTH, TM1, and TM2. (E) Electrostatic map of Cx32 HC. Cholesterol (CLR) molecules (cyan) are fitted to the lipid-2 position. (F) Detailed view of the interaction between CLR and NTH, TM1, and TM2. All the residues within 4 Å to CLR are shown as sticks. Two important residues, W3 and R22, are shown as green color.

face of the channel. The strong positive charge at the cytosolic entrance into the Cx32 HC pore may play a role in ion selectivity or gating of the channel, although it is important to note that the channel remains open in this conformation (Fig. 2E and fig. S12C).

In this context, GJCs and HCs formed by distinct connexin isoforms can discriminate for solutes based on size and charge. The selectivity filter also relies on the NTH, which contains voltage sensors that are oppositely charged in Cx32 and Cx26 (38). The voltage sensor of Cx32 has a net positive charge, whereas the voltage sensor of Cx26 has a net negative charge. In our previous work, we showed that, despite the much lower GJ conductance of single Cx32 channels with respect to Cx26 channels (28 pS versus 115 pS, respectively), the permeability to the large and negatively charged LY molecule is even higher in Cx32 than in Cx26 ($12.9 \times 10^{-3} \mu\text{m}^3/\text{s}$ versus $7 \times 10^{-3} \mu\text{m}^3/\text{s}$) (27, 45). Comparisons of Cx26,

Cx40, Cx43, and Cx45 GJ channel properties using positively and negatively charged permeants revealed that Cx26 is less permeable only to negatively charged molecules with respect to Cx43 and Cx45 (46). Thus, the structures of Cx32 along with the other GJCs and HCs provide an important structural framework for future investigations of connexin channel selectivity.

Comparison of the Cx32 GJC and HC to other connexin structures

The overall conformation of the Cx32 GJC is similar to the conformations observed in the structures of GJCs formed by Cx26, Cx46/50, and Cx43 (fig. S13A). The α - π helix transition, seen previously in the TM1 of Cx36 (35), is not observed in the corresponding regions of the Cx32 structures. The main distinction between these channel structures is the NTH region. The NTH domains of

Cx26 and Cx46/50 are structured and point deeply into the pore. The NTH of Cx43 points toward the center of the pore, closing the gate. The NTH of Cx32 is flexible, and we only observe a weak density at the position corresponding to the NTH of Cx26 and Cx46/50 (Fig. 2A and fig. S13A).

The recently determined structure of the Cx31.3 HC revealed a “semiclosed” conformation of the gate, wherein the NTH points to the middle of the pore (the diameter is about 8 Å) (fig. S13B), similar to the Cx43 GJC. Compared to Cx31.3 and Cx43, the NTH of Cx32 HC arranges itself parallel to the membrane plane but pointing toward the adjacent connexin subunit. This conformation is reminiscent of an iris-like structure in the hexameric NTH arrangement (Fig. 2, C and D).

Lipid decoration of Cx32 GJC and HC

As has been observed in the structures of Cx31.3, Cx46/50, and Cx43 (33, 34, 37), the Cx32 maps (GJC and HC) feature lipid-like densities at the protein-lipid interface (Fig. 1, B and C). Our Cx32 protein was solubilized from the HEK293 cell membranes using a mixture of *N*-dodecyl- β -D-maltopyranoside (DDM) and a cholesterol analog cholesteryl hemisuccinate (CHS), with subsequent detergent exchange to digitonin, as detailed in Materials and Methods. On the basis of the shapes of the observed densities, we interpreted them as protein-bound CHS molecules. However, it is likely that these binding sites in proximity of the hydrophobic surfaces of the protein may be occupied either by detergent molecules or by cholesterol, phospholipids, or other lipid-like molecules from the native membrane environment of Cx32. This possibility is supported by the recent structure of GJC formed by Cx46/50, which was determined in the presence of phospholipids bound at specific sites to the hydrophobic surface of Cx46/50 (33). The same is also true for our Cx43 GJC structure in lipidic environment (37). The lipids surrounding the GJCs and HCs may be important for channel assembly, stability, and function.

We also observed two lipid densities in the interior of the Cx32 HC, which we refer to as “lipid-1” and “lipid-2” (Fig. 2, B and D). Lipid-1 is aligned along the pore close to the TM1 and TM2 of both the Cx32 GJC and HC (Fig. 2, B and D), perpendicular to the membrane plane. A similar lipid density has been observed in the HC structure of Cx31.3, where it was interpreted as an LMNG molecule, suggesting it as a conserved lipid binding site. Likewise, our Cx43 structures in detergent and in nanodisc also revealed the presence of a very similar lipid molecule in the pore (37). Lipid-2 inserts to a pocket (NT pocket) formed by TM1, TM2, and NTH (Fig. 2, D to F). To simplify the interpretation of the lipid-2 site, we modeled a bound cholesterol molecule (fig. S8B). However, cholesterol, CHS, or digitonin could, in principle, match this density equally well, assuming that the headgroups are flexible and only the sterol moieties of these molecules are sufficiently ordered when bound to the lipid-2 site. The NT pocket and the bound lipid-2 molecule (Fig. 2, D to F) are specific to the Cx32 HC. The NTH is not ordered in the GJC reconstruction, and the density element corresponding to lipid-2 is missing (Fig. 2, A to D).

Structure-based insights into the pathogenesis of CMT1X

Multiple mutations in Cx32 have been found to be associated with CMT1X, and we can now locate these mutations in the experimentally determined Cx32 structures (fig. S14). Mapping of the disease-linked mutations with known molecular phenotypes can help us in

understanding the mechanism behind their deleterious effects in patients suffering from CMT1X. The Cx32 mutations can be grouped on the basis of defects related to (i) assembly and cell surface trafficking of Cx32 HCs (fig. S14, cyan), (ii) formation of GJCs (yellow), and (iii) gating mechanisms of the assembled HCs and GJCs (orange) (20). Although the defects in folding, assembly, and trafficking in certain mutants of Cx32 are difficult to explain based on the structures, our three-dimensional (3D) reconstruction allows us to explain the effects of the mutations proximal to the NTH or the NT pocket. We selected two CMT1X mutations proximal to the NTH and the NT pocket, W3S and R22G, to characterize their effect structurally and functionally. Our structures show that these two residues engage in many interactions that stabilize the NT pocket and thus likely participate in the molecular gating. The two mutants of Cx32, W3S (42) and R22G (43), have been reported to be capable of assembling the connexon and reaching the plasma membrane, without participating in functional GJs when expressed in HeLa cells and *Xenopus* oocytes, respectively. Similar to the WT Cx32, we purified the mutated proteins (fig. S3, B and C) and determined their structures using single-particle cryo-EM (figs. S4 to S6, C to F). The GJC structures of W3S and R22G were determined at 2.63- and 2.48-Å resolution, respectively. In addition to the 3D reconstructions of the mutant GJCs, we determined the structures of W3S and R22G HCs at 2.99- and 3.67-Å resolution (table S1).

Comparison of the two mutant GJC structures to the WT GJC did not reveal any obvious differences (fig. S12A): Both mutant channels showed near-identical features of the NTH density, consistent with the open state. In contrast, the W3S and R22G HCs showed stark differences to the WT Cx32 HC in the NTH region (Fig. 3, A to C, and fig. S10B). Lipid-2 is no longer present in the HC density maps of W3S and R22G, and unlike the GJC, the NTH of each of the mutants is displaced closer to the center of the pore, resulting in constriction of the central gate. The diameter of the central pore for both mutants is ~6 Å, compared to ~11 Å in the case of the WT HC (Fig. 3, A and B). Thus, under the chosen experimental conditions with proteins purified in detergent micelles, the HCs of both mutants, W3S and R22G, show a substantial closure of the NTH gate with respect to the WT channel. In contrast, the 3D reconstructions of the mutant GJCs show features similar to those found in the WT Cx32 GJC, suggesting that all of the observed GJCs are captured in an open state.

In the recently published reports analyzing the cryo-EM structures of Cx43 (36) and Cx36 GJCs (35), the individual NTH domains were shown to undergo conformational changes. To determine whether NTH behaves similarly in WT Cx32, W3S, and R22G HCs and GJCs, we performed protomer-focused classification (fig. S9A). The subunit classes of WT Cx32, W3S, and R22G GJC remained poorly resolved in the NTH region (fig. S9, B, D, and F), indicating that the NTH is flexible within the pore and does not assume distinct well-defined conformations. The NTH densities of WT Cx32 and W3S HC subunit 3D classes are ordered and resemble closely the conformation of the corresponding full HC map (fig. S9, C and E). The R22G HC protomer 3D classes are also consistent with the full refined map and indicate a presence of two possible conformations of the NTH, reminiscent of those in WT Cx32 and W3S HC, respectively (fig. S9G). However, the low resolution of the original density map currently limits the unambiguous assignment of the densities corresponding to the NTH in the R22G HC protomer-focused 3D classification.

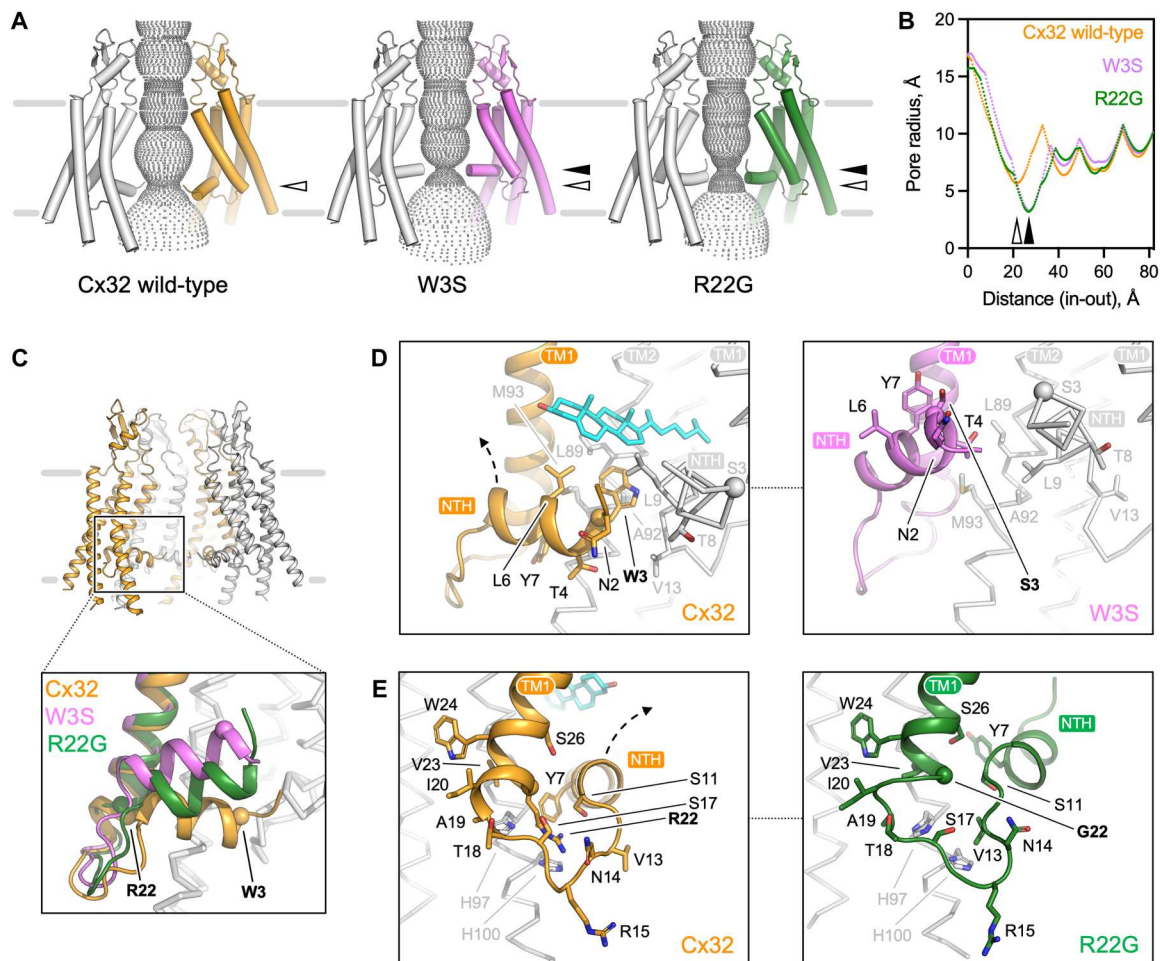


Fig. 3. Comparison of the WT Cx32 HC structure to the cryo-EM structures of W3S and R22G Cx32 mutants. (A) Substrate conduction pathways for Cx32, W3S, and R22G HCs, calculated using Hole software. The arrow indicates the narrowest part of the path. Hollow arrow for Cx32 and black arrow for mutants. (B) The pore radius along the substrate conduction pathway was calculated using hole in (A). (C) Structural alignment of NTH between Cx32 HC (orange), W3S HC (pink), and R22G HC (green). Key residues, W3 and R22, are labeled as spheres. (D and E) Detailed view of NTH in Cx32, W3S, and R22G. The key residues within 4 Å close to CLR are shown as sticks. The pink and green arrows indicate the movement of NTH in W3S and R22G compared to Cx32 HC.

Surface expression and HC dysfunction of the W3S and R22G mutants

To validate the structural observations, we performed functional assays in HEK293F and HeLa DH cells to study the permeability and gating of WT and mutant Cx32 channels. For this purpose, we used a construct containing connexin sequence followed by an internal ribosome entry site (IRES) and a cytosolic YFP to identify the transfected cells. Immunocytochemistry (ICC) experiments in both cell lines revealed that WT Cx32, W3S, and R22G localized to the plasma membrane and formed GJ plaques, observed as fluorescent lines on the plasma membrane between two cells (figs. S15 and S16). Consistent with this observation, quantification of relative plasma membrane protein expression using surface protein biotinylation followed by MS analysis showed that the levels of cell surface expression of the WT Cx32 and the two mutants were comparable (fig. S17). Despite the ability of the mutants to reach the cell surface in both HEK293F and HeLa DH cells, the properties of the GJ plaques formed by W3S and R22G in these two cell types were markedly different. In HEK293F cells, the GJ plaques formed by

the mutants were indistinguishable from those formed by the WT Cx32 (fig. S15, I and J), whereas in HeLa DH cells both mutants produced fewer and smaller GJ plaques (fig. S15, K and L).

To assess the permeability properties of WT and mutant GJ plaques, we performed patch-clamp and fluorescence recovery after photobleaching (FRAP) experiments in both HEK293F and HeLa DH cells. Although HEK293 cells have previously been reported to endogenously express Cx43 and Cx45 (47, 48), with surface biotinylation followed by MS analysis, we could confirm that under our conditions of overexpression Cx32 is the dominant connexin species in the plasma membrane of HEK293F cells. This allowed us to use these cells as a model system. In HEK293F cells, dual patch-clamp experiments indicated that the cells expressing WT Cx32 are significantly stronger coupled than control cells (Fig. 4A and fig. S18). The mutant GJs also showed a trend for higher electrical coupling compared to the control cells. We expect that the g_j values derived for both WT and mutant GJs are higher in reality, because only g_j values ranging lower than 10 to 15 nS in our measurements minimize the need for corrective

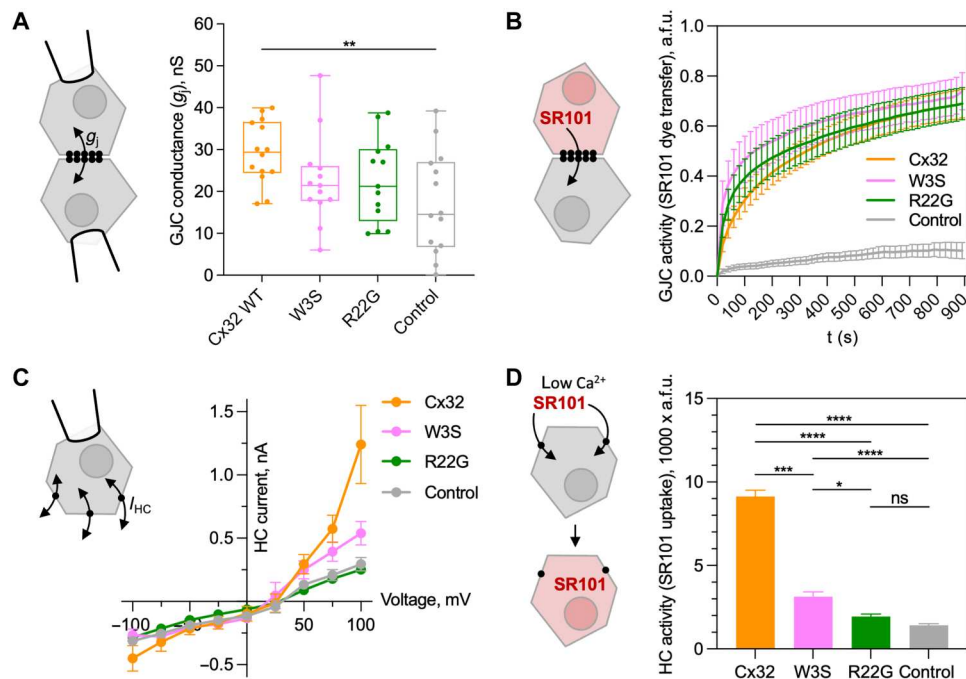


Fig. 4. Functional properties of GJCs and HCs formed by WT, W3S, or R22G Cx32 in HEK293F cells. (A) A sketch illustrating the GJC activity measurements using dual patch-clamp; black circles indicate Cx32 connexons (left). Boxplot of the GJ conductance (g_j) values measured by dual patch-clamp in untransfected (control) HEK293F cells or transfected with WT, R22G, or W3S constructs. Cell pairs were selected on the basis of similar expression of the cytosolic YFP. At the end of each experiment, g_j was lowered to zero by a CO_2 -saturated extracellular solution to confirm that the cells were connected by GJs and not by cytoplasmic bridges. g_j values of untransfected cells ($n = 14$) resulted significantly lower ($P < 0.05$) than WT ($n = 14$) but not than R22G ($n = 13$) and W3S ($n = 13$). Statistical analysis was performed using the Kruskal-Wallis test. (B) Left: FRAP experiments (sketch indicating dye transfer between two coupled cells). Inter-cellular diffusion of the fluorescent tracer SR101 (molecular weight, 606.7 Da) was assessed in control ($n = 10$) and transfected cells expressing Cx32 WT ($n = 20$), W3S ($n = 13$), or R22G ($n = 13$). (C) Left: Sketch of a whole-cell patch-clamp experiment with Cx32 HCs at the cell surface. Whole-cell patch-clamp experiments performed in control ($n = 5$) or transfected cells with Cx32 WT (orange, $n = 13$), W3S (pink, $n = 6$), or R22G (green, $n = 10$). The currents mediated by mutant HCs are lower with respect to the WT. (D) SR101 dye uptake experiments performed in control cells ($n = 935$) or cells expressing Cx32 WT ($n = 1136$), W3S ($n = 702$), or R22G ($n = 905$); mutant HCs showed reduced dye uptake; asterisks indicate statistical significance (one-way ANOVA: **** $P < 0.0001$; *** $P < 0.001$; * $P < 0.1$; ns, no significant difference). a.f.u., arbitrary fluorescence units.

methods based on electrode series and cellular input resistances (49). The same dual patch-clamp protocol performed in HeLa DH cells revealed a clear difference between the WT Cx32 and the mutants: Essentially, no coupling could be observed for the latter (fig. S18, A to C). This is likely the result of the deficient GJ plaque formation ability of the mutants in HeLa DH cells, as revealed by our ICC experiments (fig. S15). This finding highlights the dependence of GJ activity assays on the cell type and the importance of validating GJ activity data using more than one cell system.

The patch-clamp recordings were consistent with the FRAP experiments in HEK293F and HeLa DH cells (Fig. 4B and fig. S18, D to I, respectively). No significant difference in fluorescence recovery was observed between WT Cx32 and the W3S and R22G mutant expressed in HEK293F cells. In HeLa cells, only a mild permeability was observed in R22G with respect to the WT, where no recovery was found in the W3S-transfected and mock-transfected HeLa DH cells.

To assess the functional properties of the WT and mutant Cx32 HCs, we performed whole-cell patch-clamp experiments in single transfected HEK293F cells stimulated by depolarizing voltage steps (Fig. 4C and fig. S20). The results highlighted a significantly lower membrane current mediated by W3S and R22G mutants with respect to the WT HCs. These observations were in line with the

sulforhodamine 101 (SR101) dye uptake experiments performed using the same cells (Fig. 4D and fig. S21) and consistent with the reduced dimensions of the pore estimated by cryo-EM (Fig. 3).

DISCUSSION

The Cx32 structures put a spotlight on a debate about the conformation of the connexin NTH, which is involved in Cx32 connexon expression/assembly and in voltage gating (20, 40, 50). Unlike GJC structures determined previously for other connexin family members, our reconstruction of the full channel indicates that the NTH is either disordered or highly dynamic. On the basis of comparison with the HC structure, we hypothesize that the flexibility of the NTH in the GJC may occur due to the disruption of the NT pocket with the loss of a bound lipid molecule. The persistent presence of these six presumed sterol molecules inside the HC constricts the pore size and could limit the range of molecules that can permeate the HC. The previous work on connexin channel structure, including structure-function studies of Cx26, Cx46/50, and Cx31.1, led to a proposal of the NTH moving along the pore axis during the molecular gating events (28, 30, 32–34). Our structures of the WT Cx32 and W3S, R22G HCs (Fig. 3) show that the gating

mechanism may involve an iris-like movement of the NTH (Fig. 5 and movies S1 and S2).

We propose that the flexible NTH of the GJC observed in our structure is specifically required to keep the connexon in an open state configuration to allow relatively unobstructed passage of ions, second messengers, and larger diffusible molecules necessary for intercellular communication. On the basis of pore size considerations, the state of the WT Cx32 HC we derived may also be permeable to cytosolic ions and small molecules. Various cytosolic factors (including ions, small molecules, protein domains, or interaction partners) may participate in keeping the Cx32 connexon in a closed state (27, 51). For example, the open/close transitions of the "chemical/slow" gate mediated by a cytosolic Ca^{2+} sensor have been suggested to rely on a regulator molecule, such as calmodulin, directly interacting with the Cx32 NTH and acting as a cork (27, 52–54).

The observation of the NTH that forms the NT pocket filled with a lipid molecule could have important implications for the gating paradigm of connexin HCs. Minute changes in the environment of the NTH (such as binding of lipids or other small molecules within the NT pocket) may lead to rearrangement of the NTH in an iris-like fashion, as seen in the Cx32 HC structure, favoring the closure of the pore at its cytosolic side. It is known that the Cx32 channel function can be modulated by hydrophobic small molecules, such as 2-aminoethoxydiphenyl borate (55, 56), oleamide (57), or anandamide (28, 30, 32–34, 57, 58). It remains to be determined whether the NTH arrangement observed in the Cx32 HCs can be adopted by other connexin channels. Nevertheless, the possibility of manipulating the HCs or GJCs via alterations of the NT pocket opens exciting opportunities for future structure-function investigations and drug screening for the treatment of CMT1X and other connexinopathies.

Our imaging and electrophysiological experiments in W3S and R22G GJCs expressed in HeLa cells confirmed previous findings that the two mutants are not functional (42, 43), despite being capable of assembling a connexon and reaching the plasma membrane. The defect can be mainly ascribed to defective formation of GJ plaques, thus to an insufficient or null number of open channels within the GJC matrix. It should be considered that most of the channels of a GJ plaque are closed under physiological conditions, especially in small plaques where it was estimated that fewer than 2% of the channels are active (27, 59).

Previous findings related to other CMT1X mutations [e.g., R15W (41) and R22P (43)] suggested an important role of the

NTH in GJ formation. The expression level and functionality of W3S and R22G GJCs in HEK293F cells were similar to the WT, and only a reduced HC conductivity was observed, suggesting that the severity of the GJ defect is cell dependent (Fig. 4). Other Cx32 mutants, such as R75Q, M34T, V38M, R164W, Y211X, and C217X, were previously found to have a cell-dependent expression or functionality (20). This underscores the need for validating the GJ activity data in more than one cell type and, ideally, using more than one experimental technique.

The observation of both structural and functional alterations in the Cx32 mutant HCs expressed in HEK293F cells, but not in the GJCs, supports the recent hypothesis that Cx32 HC dysfunction may be implicated in the pathogenesis of CMT1X disease (19, 27). A reduced pore size in the W3S and R22G mutant HCs could conceivably impair the permeability of the channels to larger solutes such as ATP, as found in the S26L mutation (19, 60). Further studies are required to support the new paradigm for the molecular pathogenesis of CMT1X as being no longer linked to Cx32 GJCs but rather to Cx32 HCs. Direct observation of molecular defects in CMT1X-linked mutants is a crucial first step that sheds light on the therapeutic potential of rescuing dysfunctional Cx32 HCs as a personalized medicine strategy in the context of CMT1X disease onset and progression.

MATERIALS AND METHODS

Molecular cloning and mutagenesis

Human Cx32 (UniProt ID P08034), followed by a C-terminal YFP and twinStrep tag, was cloned into a pACMV plasmid. The W3S and R22G mutations were introduced using site-directed mutagenesis. For IRES containing constructs, WT untagged Cx32 and its mutants W3S and R22G were subcloned using Nhe I and Mre I into the MCS before the IRES sequence followed by YFP sequence containing pACMV vector.

Cell culture

Large-scale protein purification

HEK Freestyle 293F (HEK293F; Thermo Fisher Scientific) cells were cultured in 15-cm cell culture dishes containing Dulbecco's modified Eagle's medium (DMEM; BioConcept) supplemented with 10% fetal bovine serum (FBS) and 1% penicillin/streptomycin (PenStrep; PAN Biotech) with 5% CO_2 and cultured at 37°C. At 80% confluence, cell medium was exchanged to DMEM supplemented with 2% FBS and 1% PenStrep. The transfection mixture was

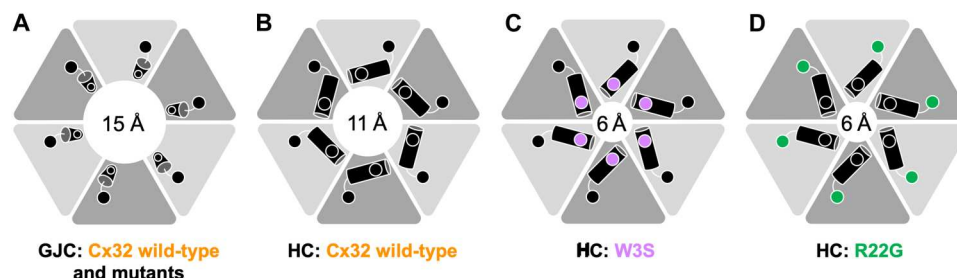


Fig. 5. A schematic illustration of the key features observed in the Cx32 structures. (A) Cx32 GJC is determined in an apparently open state, with a central pore of ~15-Å diameter; this estimate does not take into account the flexible NTH domains, as well as the lipids that may occlude the pore under physiological conditions, in the cellular plasma membrane. (B) The open state of the Cx32 HC features a central pore about 11 Å. The NTH domains are parallel to the membrane plane in an iris-like arrangement. (C and D) The W3S and R22G HC structures feature a closed state, where the NTH rearrangement reduces the pore diameter to ~6 Å.

prepared with Cx32-YFP-twinStrep plasmid and branched polyethyleneimine (Sigma-Aldrich) at a ratio of 1:2 (w/w) with serum-free DMEM. The transfection mixture was added to cells after 5 min of incubation at room temperature. After 48 hours of expression at 37°C and 5% CO₂, the cells were harvested using a cell scraper in buffer A containing 25 mM tris-HCl (pH 8.0) and 150 mM NaCl and collected by centrifugation at 800g and 4°C. The cells were washed with buffer A and collected by centrifugation. The supernatant was discarded, and the cells were frozen at –80°C for further experiments.

Surface biotinylation

HEK293F cells were cultured and transiently transfected with IRES construct as described for large-scale expression. HeLa DH cells were cultured like HEK293F cells and transiently transfected with 45 µg of IRES construct plasmid per plate using Lipofectamine 3000 (Thermo Fisher Scientific) according to the manufacturer's protocol.

IHC and Western blot

HEK293F or HeLa DH (DH clone, Sigma-Aldrich) cells were seeded on poly-L-lysine (Cultrex) precoated glass coverslips in six-well plates at a density of 0.7 million cells per well. For Western blot and whole-cell patch-clamp experiments, HEK293F cells were cultured as in ICC without the glass slide. The cell count was determined using trypan blue viability staining, and the cells were seeded in DMEM supplemented with 10% FBS and 1% PenStrep and cultured at 37°C and 5% CO₂. Twenty-four hours after seeding, HEK293F cells were transiently transfected as described above using 4 µg of DNA per well. HeLa DH cells were transiently transfected with 3 µg of DNA using Lipofectamine 3000 according to the manufacturer's protocol. The cells were placed at 37°C and 5% CO₂ for 36 hours of expression.

Dye transfer assays

For dye transfer assays in HEK293F cells, the cells were seeded and cultured as described above at 30,000 cells per well in ibidi eight-well µ-Slide chambers or 300,000 cells per ibidi µ-Dish, precoated with poly-L-lysine. Twenty-four hours after seeding, HEK293F cells were transfected as described above using 0.46 µg of DNA per well of a chamber and 2 µg of DNA per dish. The cells were placed at 37°C and 5% CO₂ for 36 hours of expression. HeLa DH cells were plated onto 12-mm-diameter glass coverslips. Twenty-four hours after plating, the cells were transiently transfected with 0.2 µg of the DNA using IRES constructs using Lipofectamine 3000 according to the manufacturer's protocol and were placed at 37°C and 5% CO₂ for 24 hours of expression.

Electrophysiology assays in HeLa cells

A clone of HeLa cells (HeLa DH) that is essentially devoid of connexins was used in our experiments. HeLa DH cells were cultured in DMEM/F12 medium (Gibco) supplemented with 10% FBS (Gibco) and 1% PenStrep at 37°C in a humidified incubator with 5% CO₂. Twenty-four hours after plating cells onto 12-mm-diameter glass coverslips, the cells were transiently transfected with 0.2 µg of the DNA of Cx32-IRES-YFP (WT) or mutant vectors (R22G or W3S) using Lipofectamine 3000 (Thermo Fisher Scientific). The mixture was added to the wells drop by drop and left to act for 4 hours, after which the medium was replaced. The mixture applied to control (Mock) cells did not contain DNA. The experiments took place 24 hours after transfection.

Electrophysiology assays in HEK293F cells

HEK293F cells were cultured in DMEM medium (Gibco) supplemented with 10% FBS (Gibco) and 1% PenStrep at 37°C in a humidified incubator with 5% CO₂. The cells were seeded onto a 24-well dish and incubated for 18 to 24 hours at 37°C until they were approximately 50 to 70% confluent. After which, the cells were transiently transfected with 0.2 µg of the DNA of Cx32-IRES-YFP (WT) or mutant vectors (R22G or W3S) using Rotifect (Carl Roth) according to the standard manufacturer's protocol. Twenty-four hours after the transfection, the cells were seeded on glass coverslips [previously coated with polyornithine (100 µg/ml) for 1 hour at room temperature]. The experiments took place 48 hours after transfection.

Cx32 purification

The cells were resuspended in buffer A supplemented with protease inhibitors [1 mM benzamide, leupeptin (1 µg/ml), aprotinin (1 µg/ml), pepstatin (1 µg/ml), trypsin inhibitor (1 µg/ml), and 1 mM phenylmethylsulfonyl fluoride]. Cells were lysed using sonication at 35% amplitude with two sonication cycles per plate (cycle: 0.5-s pulse on, 0.5-s pulse off), and the membrane preparation was clarified by ultracentrifugation at 35,000 rpm (Beckman Ti45 rotor) to remove the soluble fraction. The membrane pellet was resuspended in buffer A supplemented with protease inhibitors using a homogenizer. The membranes were solubilized by adding 1% N-Dodecyl-β-D-maltoside (DDM) and 0.2% cholesteryl hemisuccinate (CHS) and incubated at 4°C for 1 hour. The solubilized membranes were centrifuged by an additional round of ultracentrifugation. The supernatant was incubated with 1 ml of CNBr-activated Sepharose-coupled anti-GFP nanobody (61) at 4°C. The resin and protein mixture was collected in a gravity column and washed with 40 column volumes of buffer B [25 mM tris-HCl (pH 8.0), 150 mM NaCl, and 0.1% digitonin]. Protein was cleaved overnight at 4°C by adding 0.4 mg of human rhinovirus 3C protease. The Cx32 protein was collected and concentrated to 1 ml using a 100-kDa cutoff concentrator. The Cx32 sample was injected onto a Superose 6 Increase 10/300 GL column preequilibrated with buffer B. The Cx32 peak fractions were collected, concentrated, and used for cryo-EM grid preparation immediately. The expression and purification methods of W3S and R22G mutants were the same as the WT.

Cryo-EM sample preparation and data collection

The purified Cx32 WT protein, W3S, and R22G were concentrated to about 5 mg/ml. The cryo-EM grids were glow-discharged for 30 s using a PELCO easiGlow glow discharge system. Protein (3.5 µl) was added to the glow-discharged Quantifoil R1.2/1.3 200-mesh grid. The grids were blotted using VitroBot Mark IV (Thermo Fisher Scientific) and plunge-frozen in liquid ethane (blot force, 10; blot time, 3 s). The grids were transferred to liquid nitrogen for storage and cryo-EM data collection. Cryo-EM datasets were collected using a Titan Krios electron microscope equipped with a K3 direct electron detector (Gatan) and a GIF Quantum energy filter (slit width of 20 eV) at ScopeM, ETH Zurich. The defocus range was set from –1.0 to –2.0 µm. The micrographs were collected using EPU2.0 software and dose-fractionated to 40 frames in superresolution mode. The exposure time for each micrograph was 0.7 s, and the total dose was about 50 e[–]/Å².

Cryo-EM data processing

The images were classified into groups using a script provided by P. Afanasyev (ETH Zurich; <https://github.com/afanasyevp/afis>, version aee8f66, 27 May 2021). The movies were first binned twofold and motion-corrected using MotionCor2 (62). The nominal pixel size of the micrograph after twofold binning was 0.678 Å. Gctf (63) was used for CTF estimation. About 1000 particles were manually picked in Relion3.1 (64, 65). A 2D classification of the manually picked particles showed clear features of GJCs and HCs. The selected 2D classes were used as templates to autopick the particles in all micrographs using Relion3.1. After several rounds of 2D classification, the GJCs and HCs were selected separately based on their features and transferred to Cryosparc2 (66) to generate the initial models. W3S and R22G were processed using Cx32 as initial model. A 3D classification of GJCs and HCs was performed separately in Relion3.1. The good 3D classes for GJCs and HCs were selected for further 3D refinement. CTF refinement and particle polishing were also performed using Relion3.1 to further improve the resolution. The calibrated pixel size was corrected to 0.654 Å during postprocessing. Local resolution maps were calculated using ResMap (67) implemented in Relion3.1. The detailed steps of image processing are shown in figs. S4 to S8 and table S1.

Protomer-focused classification was performed as described previously (36). Briefly, the particles were symmetry expanded using the "relion_particle_symmetry_expand" command, using D6 or C6 symmetry for GJCs and HCs, respectively. The refined maps of full GJCs or HCs were used as consensus maps to generate the subunit references in Chimera (68), based on the respective model, using the "Color Zone" and "Split Map" commands. The subunit references were used to generate the respective masks by low-pass filtering to 10 Å, extending the map by 5 pixels and adding a soft edge of 20 pixels. Particle subtraction was performed on the symmetry-expanded particles, which were recentered and rescaled to 200 × 200 pixels. The 3D classification was performed on subtracted particles using the subunit reference and mask without particle alignment using four, six, or eight classes. The classifications with different class numbers were judged by evaluating whether higher class number revealed additional defined conformational differences between protomers in NTH and lipid 1 and 2 sites. The detailed steps of protomer-focused classification are shown in fig. S9.

Model building and refinement

Model building was carried out manually in Coot (69). Connexin26 structure [Protein Data Bank (PDB) ID: 2ZW3] was used as a guide template, and the side chains of the bulky residues (Phe, Trp, Tyr, and Arg) were used as a guide for model building. The models were refined using `real_space_refine` in Phenix (70). The models were validated as previously described (71). The atoms of the refined model were randomly displaced by 0.5 Å using PDB tools implemented in Phenix. This perturbed model was refined against the half map1. The new refined model was used to generate an Fourier Shell Correlation (FSC) curve of model versus half map2. The geometries of the model were validated using MolProbity (72). All figures were prepared in PyMOL (73), Chimera (68), and ChimeraX (74).

MS analysis of purified Cx32 protein N terminus

Sample preparation for liquid chromatography–tandem MS (LC-MS/MS) analysis

Protein (2 µg; Cx32, W3S, and R22G) was digested using ProtiFi S-Trap microcolumns according to the manufacturer's instructions. The peptides were dried in a vacuum centrifuge and resuspended in 5% acetonitrile (ACN), 0.1% formic acid (FA).

LC-MS/MS data acquisition

The sample was injected and analyzed on an Orbitrap Exploris 480 mass spectrometer, equipped with a nanoelectrospray source and coupled to Easy-nLC 1200 (Thermo Fisher Scientific). Peptides were separated with a 60-min gradient from 3 to 30% B [eluent A: 0.1% FA and eluent B: 95% ACN, 0.1% FA] on a 40 cm × 0.75 µm in-house packed C18 column (3-µm C18 beads, Dr. Maisch Pronto-SIL), heated to 50°C. The three samples were measured in a data-independent acquisition (DIA) method mode using 41 fragmentation windows with 1 mass/charge ratio (m/z) overlap. MS1 scan range was set to 350 to 1150 m/z with a normalized automatic gain control (AGC) target of 200% and radio frequency (RF) value of 50%. The maximum injection time was set to 264 ms, and the Orbitrap resolution was set to 120,000. For MS2 scans, the normalized AGC target was set to 200%, the maximum injection time was 66 ms, RF lens was set to 50%, and the collision energy was set to 30%. The total method length was 72 min.

Data analysis

The acquired raw files were analyzed with Spectronaut (Biognosys) version 15.7 in directDIA mode. Default settings were used, except that indexed retention time (iRT) calibration, cross run normalization, and imputation were switched off and single hits were excluded. For identification, a FASTA file of the human proteome [downloaded from UniProt (75)], a FASTA file with all Cx32 sequences (mutations and WT), and a contaminant FASTA file [MaxQuant (76)] were used. Plots were made in R version 4.1.1 using the R packages tidyverse (77) and protti (78). Raw files, file annotations, FASTA files, and search results have been deposited on PRIDE (79): PXD039379 (surface biotinylation, HeLa DH), PXD033848 (purified protein analysis), and PXD033671 (surface biotinylation, HEK293F).

Surface protein biotinylation

Cell surface protein biotinylation was done using the Pierce Cell Surface Biotinylation and Isolation Kit (Thermo Fisher Scientific) according to the manufacturer's protocol. The eluted surface biotinylated proteins were analyzed using MS.

MS analysis of surface protein biotinylation, HEK293F cells

Sample preparation for LC-MS/MS analysis

One hundred microliters of each eluted sample was digested using ProtiFi S-Trap microcolumns with a few modifications of the manufacturer's protocol. Briefly, disulfide bonds did not have to be reduced with dithiothreitol (DTT) as the elution buffer already contained DTT. Fifty microliters of 2× lysis buffer [10% SDS and 100 mM triethyl ammonium bicarbonate (TEAB) (pH 7.55)] was added, and free cysteines were alkylated with 40 mM iodoacetamide. The rest of the sample preparation was conducted as recommended by the manufacturer. After drying, the peptides were resuspended in 30 µl of 5% ACN, 0.1% FA with an addition of iRT peptides (Biognosys). For library generation, pooled samples of each condition

were measured with a data dependent acquisition (DDA) method and included alongside all DIA measurements of all samples.

LC-MS/MS data acquisition, DDA measurements

Peptides from pooled samples of each condition were separated with a linear gradient from 3 to 35% B (eluent A: 0.1% FA in water and eluent B: 0.1% FA in ACN) on an in-house packed 40 cm × 0.75 μm C18 column (1.9-μm C18 beads, Dr. Maisch Repronil-Pur) connected to an Acquity UPLC M-Class system (Waters). Samples were acquired on an Orbitrap Fusion Lumos Tribrid mass spectrometer (Thermo Fisher Scientific) at a normalized AGC target of 200% for both MS1 and MS2. The scan range was set to 350 to 1150 *m/z*, RF lens was set to 30%, and the maximum injection time was 100 ms for MS1 and 54 ms for MS2. Cycle time was 3 s, and the dynamic exclusion was set to 60 s. Charge states between 2 and 7 were acquired, and the Orbitrap resolution for MS1 was set to 120,000 and 30,000 for MS2. Peptides were fragmented with higher-energy collisional dissociation (HCD) at a collision energy of 30%. The total method length was 165 min.

LC-MS/MS data acquisition, DIA measurements

Peptides were separated on a similar gradient from 3 to 35% B and a total method length of 165 min. MS1 scan range was set to 250 to 1400 *m/z*, and RF lens was set to 30%. Normalized AGC target was 50%, and the maximum injection time for MS1 was 100 ms. MS1 Orbitrap resolution was 120,000, and MS2 Orbitrap resolution was set to 30,000. Peptides were fragmented in 41 sequential windows with 1 *m/z* overlap, with a maximum injection time of 54 ms. HCD collision energy was set to 28%.

Data analysis

Spectronaut version 15.7 was used for data analysis. Libraries were generated from all samples measured in DDA and DIA. CAMthio-propanoylation (+145.02 Da) was included as a variable post-translational modification (PTM), trypsin/P, and Lys-C/P were set as digestion enzymes. The samples were searched against sequences of the human proteome [downloaded from UniProt (75)], mutated and nonmutated Cx32, CFP, and a FASTA file of common contaminants [MaxQuant (76)]. Peptides identified in mutated regions were excluded from the quantification. The minimum peptide length was set to five amino acids. During the search, single hits were excluded and PTM localization was conducted. Missing values were not imputed. Data were exported from Spectronaut and further analyzed in R version 4.1.1 using the R packages tidyverse (77), protti (78), and ggpubr (80). Raw files, file annotations, FASTA files, spectral library, search results, and the data analysis script are deposited on PRIDE (PXD033671).

MS analysis of surface protein biotinylation, HeLa cells

Sample preparation for LC-MS/MS analysis

Fifty microliters of each sample was digested with ProtiFi S-Trap microcolumns as mentioned above. Pooled samples of each condition were prepared for DDA library measurements, and nonbiotinylated control samples were included to exclude proteins that could show unspecific binding.

LC-MS/MS data acquisition, DDA measurements

Peptides from pooled samples of each condition were separated with a linear gradient from 3 to 30% B (eluent A: 0.1% FA in water and eluent B: 95% ACN and 0.1% FA) on an in-house packed 40 cm × 0.75 μm C18 column (3-μm C18 beads, Dr. Maisch ProntoSIL) connected to Easy-nLC 1200 (Thermo Fisher Scientific). Measurements were acquired on a Orbitrap Exploris

480 mass spectrometer (Thermo Fisher Scientific) at a normalized AGC target of 200% for both MS1 and MS2. The scan range was set to 350 to 1150 *m/z*, RF lens was set to 50%, and the maximum injection time was 264 ms for MS1 and 54 ms for MS2. Twenty dependent scans were acquired, and dynamic exclusion was set to 20 s. Charge states between 2 and 6 were selected, and the Orbitrap resolution for MS1 was set to 120,000 and 30,000 for MS2. Peptides were fragmented with HCD at a collision energy of 30%. The total method length was 132 min.

LC-MS/MS data acquisition, DIA measurements

All samples (biotinylated samples and nonbiotinylated controls) were measured in DIA. Peptides were separated on a similar gradient from 3 to 30% B and a total method length of 132 min. MS1 scan range was set to 350 to 1150 *m/z*, and RF lens was set to 50%. Normalized AGC target was 200% and the maximum injection time for MS1 was 264 ms. MS1 Orbitrap resolution was set to 120,000, and MS2 Orbitrap resolution was set to 30,000. Peptides were fragmented in 41 sequential windows with 1 *m/z* overlap, with a maximum injection time of 66 ms. HCD collision energy was set to 30%. A lock-mass (445.12003 *m/z*) was included for internal mass calibration.

Data analysis

Data were analyzed as mentioned above, except that nonbiotinylated samples were searched and the identified proteins (unspecific binders) were excluded from the analysis.

Western blot analysis

Cells, analyzed for total protein expression, were washed with 1× phosphate-buffered saline (PBS), trypsinized with 500 μl of trypsin-EDTA (BioConcept) for 5 min, resuspended in 500 μl of ice-cold DMEM supplemented with 10% FBS and 1% PenStrep, and transferred to a microcentrifuge tube. The cells were pelleted by centrifugation for 20 min at 1000 rpm at 4°C, and the supernatant was discarded. The pellet was resuspended in 150 mM NaCl, 50 mM tris-HCl (pH 8.0) supplemented with deoxyribonuclease I. The cells were sonicated for five cycles as described in protein purification, and the cells were diluted in 4× SDS-polyacrylamide gel electrophoresis loading buffer.

Immunocytochemistry

The cells were fixed on a glass coverslip with 4% formaldehyde in 1× PBS at room temperature for 20 min and washed twice with 1× PBS. In experiments evaluating protein localization, the plasma membrane was additionally stained with Vybrant CM-DiI (Invitrogen) for 10 min, washed three times with 1× PBS, and fixed again as described above. The coverslips were transferred to buffer containing 5% urea (w/v), 100 mM Tris-HCl (pH 8.0) at 95°C for 10 min for antigen retrieval. The coverslips were washed three times with 1× PBS for 5 min and then placed in 1× PBS containing 100 μM digitonin for 10 min for membrane permeabilization, followed by the same washing procedure as described above. The coverslips were then incubated in 1% bovine serum albumin (BSA), glycine (22.52 mg/ml) in PBST (0.1% Tween 20) buffer for 30 min and then transferred to 1% BSA in PBST buffer containing rabbit polyclonal anti-Cx32 antibody (#34-5700, Invitrogen) at a 1:250 dilution in a humidified chamber at 4°C for overnight incubation. The coverslips were again washed three times by 5-min incubation in 1× PBS and transferred to 1% BSA PBST buffer containing goat anti-rabbit immunoglobulin G Alexa Fluor 488-conjugated secondary

antibody (ab150077, Abcam) at 1:1000 dilution for protein localization assessment or goat anti-rabbit Alexa Fluor 647–conjugated secondary antibody (ab150079, Abcam) at 1:2000 dilution for connexin and YFP coexpression assessment. The cells were then washed three times with PBS for 5 min, stained with Hoechst 33342 fluorescent dye (50 µg/ml; Sigma) in 1× PBS for 1 min, washed once with 1× PBS, and then mounted on glass slides using gelvatol. The samples were stored at 4°C before imaging.

Dye transfer assays

For dye uptake assays in HEK293F cells, the cells were washed twice with PBS-E (1× PBS–5 mM EDTA) and preincubated with PBS-E for 5 min. PBS-E was then replaced with PBS-E containing SR101 (50 µg/ml; Sigma) and incubated for 5 min for HC dye uptake assay and 15 min for GJC FRAP assay. After incubation, the cells were washed four times with 1× PBS and imaged in FluoroBrite DMEM supplemented with 1% FBS and 1% PenStrep.

For dye uptake experiments in HeLa DH cells, the cells were loaded with 10 µM Calcein Blue AM (Invitrogen) dye in DMEM/F12 medium in the presence of 25 µM sulfapyrazone (Sigma-Aldrich) and 0.1% of Pluronic F-127 (Invitrogen) and incubated at 37°C in a humidified incubator with 5% CO₂ for 30 min, before imaging in an extracellular solution containing 150 mM NaCl, 10 mM Hepes, 5 mM KCl, 5 mM glucose, 1 mM MgCl₂, 2 mM CaCl₂, and 2 mM sodium pyruvate (pH 7.4, 311 mOsm).

Light microscopy

ICC and HEK293F dye transfer assay samples were imaged using a Leica STELLARIS 5 confocal microscope using LAS X (4.2.1.23819—build 23180) acquisition software. The overview images, where applicable, were acquired using an HC PL APO 20×/0.75 dry objective, and the images for data analysis with an HC PL APO 63×/1.4 oil CS2 objective and a pinhole airy of 1.06 Airy Units (AU) (101.4 µm), pixel dwell time of 3.1625 µs, and a scan speed of 400 Hz. The images were collected using the 405-, 488-, 561-, and 638-nm laser lines for Hoechst 33342, EYFP and Alexa Fluor 488, SR101 and CM-DiI, and Alexa Fluor 647 fluorescent dyes, respectively, with a frame sequential data acquisition scheme and detected with a HyD camera detector.

ICC samples

For GJ characterization, overview images of the whole coverslip were collected with 10% overlap and stitched in the acquisition software. The positions for data collection were distributed evenly over the whole surface where respective connexin and plasma membrane signals were present to avoid bias as well as target transfected cells. Z-stacks of 7 µm were collected with a z step of 0.3 µm from the defined positions, with the center of each stack determined as the z height with the highest signal from the nucleus. For nonquantitative ICC samples, the data were collected without prior overview acquisition.

HC dye uptake assays in HEK293F cells

Ten images were collected per condition, and each condition was imaged using the same microscope image acquisition settings. Each assay was done in experimental triplicates.

GJC FRAP assays in HEK293F cells

The YFP fluorescence was used to identify transfected cells. Neighboring cells with YFP fluorescence were selected as regions for FRAP experiment. A cell bordering to other cells is defined as the region of interest (ROI) and bleached with 100% SR101 laser line intensity after collecting six prebleach images at a lower SR101 laser line intensity in 5.16-s intervals. After bleach pulses, the fluorescence recovery was recorded at the lower SR101 laser line intensity every 20.16 s for 45 frames, where the dye recovery reached plateau.

GJC FRAP assays in HeLa DH cells

The cells were mounted on the stage of an upright wide-field fluorescence microscope (Olympus BX51WI) with an infinity-corrected water immersion objective [40×, 0.8 numerical aperture (NA), Olympus]. Cytosolic YFP fluorescence was excited by a 470-nm light-emitting diode (LED), while Calcein Blue fluorescence was excited by a 365-nm LED. Isolated pairs of Cx32-transfected HeLa cells were selected on the basis of their cytosolic YFP expression. A 375-nm UV laser beam was focalized for 300 ms on one cell of the pair to bleach its Calcein Blue content and observe the following recovery mediated by passive diffusion of Calcein Blue through Cx32 GJs connecting the cell pair.

Light microscopy image analysis

GJ characterization

Stacks collected from the same region but with different channels were imported in Fiji and merged. Connexin signal was considered as a GJ if it colocalized with the plasma membrane stain and was present in three or more stack slices. The GJs were counted and measured from the longest slice manually. The measurements were exported to GraphPad Prism and compared using one-way analysis of variance (ANOVA), followed by Tukey's multiple comparisons test.

HC dye transfer assays in HEK293F cells

Images were processed using a Python script (<https://github.com/lavrihap/hc-data-processing.git>, version 1944bae, 15 March 2022). The values were imported to GraphPad Prism 9.0.0 for analysis. The replicates were combined and plotted as means ± SEM. The significance of dye uptake difference between different conditions was assessed using ordinary one-way ANOVA and Games-Howell's multiple comparisons test.

GJC FRAP dye transfer assays in HEK293F cells

FRAP images were imported in Fiji, and pixel intensities in the time series were measured from three regions: bleached cell (ROI1), neighboring cells including the bleached cell (ROI2), and background (ROI3). The fluorescence recovery curves were calculated with EasyFRAP-web software (81) using full-scale normalization, and the normalized curves were exported to GraphPad Prism. All curves were plotted, and a one-way association curve was fitted to the data. The percentage of FRAP recovery was determined and compared using ordinary one-way ANOVA and Tukey's multiple comparisons test with a single pooled variance.

GJC FRAP dye transfer assays in HeLa DH cells

Data were analyzed using a software we developed in MATLAB (The MathWorks Inc.).

Electrophysiology**Dual patch-clamp electrophysiological experiments in HeLa DH and HEK293F cells**

A glass coverslip of Cx32-IRES-YFP (WT) or mutant (R22G or W3S) transfected cells was transferred to an experimental chamber at room temperature (22° to 24°C) and mounted on the stage of an upright wide-field fluorescence microscope (Olympus BX51WI) with an infinity-corrected water immersion objective (40×, 0.8 NA, Olympus). We continuously superfused the cells at the rate of 2 ml/min with an extracellular solution containing 130 mM NaCl, 10 mM Hepes, 5 mM KCl, 5 mM glucose, 1 mM MgCl₂, 2 mM CaCl₂, 2 mM sodium pyruvate, 4 mM tetraethylammonium chloride (TEAC), 4 mM CsCl, 2 mM 4-aminopyridine, 2 μM 1-[(2-Chlorophenyl)diphenylmethyl]-1H-pyrazole (TRAM-34), and 400 nM (UCL-1684) (pH 7.4, 318 mOsm). Cytosolic YFP fluorescence was excited by a 470-nm LED to identify the transfected cells and allow subsequent electrophysiological analysis. Patch-clamp recordings were performed using an Axon 700B amplifier (Molecular Device) with a dual headstage configuration capable of carrying out simultaneous measurements. Pipettes were filled with an intracellular solution containing 125 mM potassium aspartate (KAsp), 10 mM NaCl, 10 mM Hepes, 13 mM KCl, 1 mM MgCl₂, and 50 μM 1,2-bis(2-aminophenoxy)ethane-*N,N,N',N'*-tetraacetic acid (pH 7.2, 309 mOsm) filtered through a 0.22-μm pore size membrane (Millipore). The resistance of patch pipettes in the bath ranged between 6 and 8 megohms. Once the whole-cell configuration was achieved, both cells were voltage-clamped at -20 mV. The junctional current I_j was measured in cell 1 by applying voltage steps $V_j = +10$ mV to cell 2. The corresponding junctional conductance was computed as $g_j = I_j/V_j$. At the end of almost all experiments, we applied CO₂ to the bath to prove that junctional currents occurred through Cx32 GJ WT or mutant channels. Electrophysiological data were acquired by pClamp software (version 10.4, Molecular Device) and analyzed with a software we developed in MATLAB (The MathWorks Inc.).

Whole-cell patch-clamp experiment

HC activity was measured using whole-cell patch-clamp with an EPC10 amplifier (HEKA, Germany). Data were acquired at a 1-ms sampling rate and filtered at 3 kHz. Isolated cells expressing Cx32, W3S, and R22G were patched. Cells were continuously perfused with extracellular solution containing 140 mM NaCl, 5.4 mM CsCl, 1.8 mM CaCl₂, 1 mM MgCl₂, 2 mM BaCl₂, and 10 mM Hepes (~310 mOsm) at pH 7.4 adjusted with NaOH. CsCl (5.4 mM) and BaCl₂ (2 mM) were added to suppress Na⁺-K⁺-adenosine triphosphatase pump activities and Ca²⁺-activated K⁺ channel currents. Patch pipettes were pulled from borosilicate glass at a resistance of 3 to 4 megohms and filled with intracellular solution containing 130 mM CsCl, 10 mM Na gluconate, 0.26 mM CaCl₂, 1 mM MgCl₂, 2 mM EGTA, 7 mM TEAC, and 5 mM Hepes (~300 mOsm) at pH 7.2 adjusted with CsOH. CsCl (130 mM) was added, where Cs⁺ was the sole charge carrier that does not mediate outward current through K⁺ channels and TEA-Cl was used to block residual K⁺-currents. All recordings were performed at room temperature. After 45 to 60 s of whole-cell giga seal configuration, the HC activity was measured with voltage steps $\Delta V = 25$ mV from -100 to +100 mV, which was applied for every 1 s for 10 s. Data were analyzed using fit master (HEKA, Germany), and peak amplitudes were measured to generate the *I-V* curve. Statistical analysis on peak

amplitude current at different voltage steps was performed using ordinary one-way ANOVA and Sidak's test. Data are presented as means ± SEM.

Supplementary Materials**This PDF file includes:**

Figs. S1 to S21

Table S1

Legends for movies S1 and S2

Other Supplementary Material for this manuscript includes the following:

Movies S1 and S2

REFERENCES AND NOTES

1. M. Goldberg, M. De Pitta, V. Volman, H. Berry, E. Ben-Jacob, Nonlinear gap junctions enable long-distance propagation of pulsating calcium waves in astrocyte networks. *PLOS Comput. Biol.* **6**, e1000909 (2010).
2. S. Rohr, Role of gap junctions in the propagation of the cardiac action potential. *Cardiovasc. Res.* **62**, 309–322 (2004).
3. I. Epifantseva, R. M. Shaw, Intracellular trafficking pathways of Cx43 gap junction channels. *Biochim. Biophys. Acta Biomembr.* **1860**, 40–47 (2018).
4. D. C. Spray, R. Iglesias, N. Shraer, S. O. Suadicani, V. Belzer, R. Hanstein, M. Hanani, Gap junction mediated signaling between satellite glia and neurons in trigeminal ganglia. *Glia* **67**, 791–801 (2019).
5. P. Meda, Gap junction proteins are key drivers of endocrine function. *Biochim. Biophys. Acta Biomembr.* **1860**, 124–140 (2018).
6. J. Neijssen, B. Pang, J. Neefjes, Gap junction-mediated intercellular communication in the immune system. *Prog. Biophys. Mol. Biol.* **94**, 207–218 (2007).
7. P. Wong, V. Laxton, S. Srivastava, Y. W. Chan, G. Tse, The role of gap junctions in inflammatory and neoplastic disorders (Review). *Int. J. Mol. Med.* **39**, 498–506 (2017).
8. M. Sinyuk, E. E. Mulkearns-Hubert, O. Reizes, J. Lathia, Cancer connectors: Connexins, gap junctions, and communication. *Front. Oncol.* **8**, 646 (2018).
9. A. B. Belousov, J. D. Fontes, M. Freitas-Andrade, C. C. Naus, Gap junctions and hemichannels: Communicating cell death in neurodevelopment and disease. *BMC Cell Biol.* **18**, 4 (2017).
10. M. Srinivas, V. K. Verselis, T. W. White, Human diseases associated with connexin mutations. *Biochim. Biophys. Acta Biomembr.* **1860**, 192–201 (2018).
11. G. Sohl, K. Willecke, Gap junctions and the connexin protein family. *Cardiovasc. Res.* **62**, 228–232 (2004).
12. D. A. Goodenough, D. L. Paul, Gap junctions. *Cold Spring Harb. Perspect. Biol.* **1**, a002576 (2009).
13. W. H. Evans, E. De Vuyst, L. Leybaert, The gap junction cellular internet: Connexin hemichannels enter the signalling limelight. *Biochem. J.* **397**, 1–14 (2006).
14. D. L. Paul, Molecular cloning of cDNA for rat liver gap junction protein. *J. Cell Biol.* **103**, 123–134 (1986).
15. S. S. Scherer, S. M. Deschenes, Y. T. Xu, J. B. Grinspan, K. H. Fischbeck, D. L. Paul, Connexin32 is a myelin-related protein in the PNS and CNS. *J. Neurosci.* **15**, 8281–8294 (1995).
16. J. E. Rash, T. Yasumura, F. E. Dudek, J. I. Nagy, Cell-specific expression of connexins and evidence of restricted gap junctional coupling between glial cells and between neurons. *J. Neurosci.* **21**, 1983–2000 (2001).
17. C. Meier, R. Dermietzel, K. G. Davidson, T. Yasumura, J. E. Rash, Connexin32-containing gap junctions in Schwann cells at the internodal zone of partial myelin compaction and in Schmidt-Lanterman incisures. *J. Neurosci.* **24**, 3186–3198 (2004).
18. R. J. Balice-Gordon, L. J. Bone, S. S. Scherer, Functional gap junctions in the schwann cell myelin sheath. *J. Cell Biol.* **142**, 1095–1104 (1998).
19. A. Nualart-Marti, E. M. del Molino, X. Grandes, L. Bahima, M. Martin-Satué, R. Puchal, I. Fasciani, D. González-Nieto, B. Ziganshin, A. Llobet, L. C. Barrio, C. Solsóna, Role of connexin 32 hemichannels in the release of ATP from peripheral nerves. *Glia* **61**, 1976–1989 (2013).
20. M. Bortolozzi, What's the function of connexin 32 in the peripheral nervous system? *Front. Mol. Neurosci.* **11**, 227 (2018).
21. L. J. Bone, S. M. Deschenes, R. J. Balice-Gordon, K. H. Fischbeck, S. S. Scherer, Connexin32 and X-linked Charcot-Marie-Tooth disease. *Neurobiol. Dis.* **4**, 221–230 (1997).

22. S. Gupta, T. Benstead, P. Neumann, D. Guernsey, A point mutation in codon 3 of connexin-32 is associated with X-linked Charcot-Marie-Tooth neuropathy. *Hum. Mutat.* **8**, 375–376 (1996).
23. V. V. Ionasescu, X-linked Charcot-Marie-Tooth disease and connexin32. *Cell Biol. Int.* **22**, 807–813 (1998).
24. K. A. Kleopa, C. K. Abrams, S. S. Scherer, How do mutations in GJB1 cause X-linked Charcot-Marie-Tooth disease? *Brain Res.* **1487**, 198–205 (2012).
25. S. J. Fleishman, V. M. Unger, M. Yeager, N. Ben-Tal, A Calpha model for the transmembrane alpha helices of gap junction intercellular channels. *Mol. Cell* **15**, 879–888 (2004).
26. S. Pantano, F. Zonta, F. Mammano, A fully atomistic model of the Cx32 connexon. *PLOS ONE* **3**, e2614 (2008).
27. A. Carrer, A. Leparulo, G. Crispino, C. D. Ciubotaru, O. Marin, F. Zonta, M. Bortolozzi, Cx32 hemichannel opening by cytosolic Ca²⁺ is inhibited by the R220X mutation that causes Charcot-Marie-Tooth disease. *Hum. Mol. Genet.* **27**, 80–94 (2018).
28. S. Maeda, S. Nakagawa, M. Suga, E. Yamashita, A. Oshima, Y. Fujiyoshi, T. Tsukihara, Structure of the connexin 26 gap junction channel at 3.5 Å resolution. *Nature* **458**, 597–602 (2009).
29. A. Oshima, K. Tani, Y. Hiroaki, Y. Fujiyoshi, G. E. Sosinsky, Three-dimensional structure of a human connexin26 gap junction channel reveals a plug in the vestibule. *Proc. Natl. Acad. Sci. U.S.A.* **104**, 10034–10039 (2007).
30. B. C. Bennett, M. D. Purdy, K. A. Baker, C. Acharya, W. E. McIntire, R. C. Stevens, Q. Zhang, A. L. Harris, R. Abagyan, M. Yeager, An electrostatic mechanism for Ca²⁺-mediated regulation of gap junction channels. *Nat. Commun.* **7**, 8770 (2016).
31. A. K. Khan, M. Jagielnicki, W. E. McIntire, M. D. Purdy, V. Dharmarajan, P. R. Griffin, M. Yeager, A steric “ball-and-chain” mechanism for pH-mediated regulation of gap junction channels. *Cell Rep.* **31**, 107482 (2020).
32. J. B. Myers, B. G. Haddad, S. E. O’Neill, D. S. Chorev, C. C. Yoshioka, C. V. Robinson, D. M. Zuckerman, S. L. Reichow, Structure of native lens connexin 46/50 intercellular channels by cryo-EM. *Nature* **564**, 372–377 (2018).
33. J. A. Flores, B. G. Haddad, K. A. Dolan, J. B. Myers, C. C. Yoshioka, J. Copperman, D. M. Zuckerman, S. L. Reichow, Connexin-46/50 in a dynamic lipid environment resolved by CryoEM at 1.9 Å. *Nat. Commun.* **11**, 4331 (2020).
34. H. J. Lee, H. Jeong, J. Hyun, B. Ryu, K. Park, H. H. Lim, J. Yoo, J. S. Woo, Cryo-EM structure of human Cx31.3/GJC3 connexin hemichannel. *Sci. Adv.* **6**, eaba4996 (2020).
35. S. N. Lee, H. J. Cho, H. Jeong, B. Ryu, H. J. Lee, M. Kim, J. Yoo, J. S. Woo, H. H. Lee, Cryo-EM structures of human Cx36/GJD2 neuronal gap junction channel. *Nat. Commun.* **14**, 1347 (2023).
36. H. J. Lee, H. J. Cha, H. Jeong, S. N. Lee, C. W. Lee, M. Kim, J. Yoo, J. S. Woo, Conformational changes in the human Cx43/GJA1 gap junction channel visualized using cryo-EM. *Nat. Commun.* **14**, 931 (2023).
37. C. Qi, S. Acosta Gutierrez, P. Lavriha, A. Othman, D. Lopez-Pigozzi, E. Bayraktar, D. Schuster, Paola Picotti, N. Zamboni, M. Bortolozzi, F. L. Gervasio, V. M. Korkhov, Structure of the connexin-43 gap junction channel in a putative closed state. *eLife* **12** (2023); 10.7554/eLife.87616.
38. S. Oh, S. Rivkin, Q. Tang, V. K. Verselis, T. A. Bargiello, Determinants of gating polarity of a connexin 32 hemichannel. *Biophys. J.* **87**, 912–928 (2004).
39. P. E. Purnick, D. C. Benjamin, V. K. Verselis, T. A. Bargiello, T. L. Dowd, Structure of the amino terminus of a gap junction protein. *Arch. Biochem. Biophys.* **381**, 181–190 (2000).
40. P. E. Purnick, S. Oh, C. K. Abrams, V. K. Verselis, T. A. Bargiello, Reversal of the gating polarity of gap junctions by negative charge substitutions in the N-terminus of connexin 32. *Biophys. J.* **79**, 2403–2415 (2000).
41. C. K. Abrams, M. M. Freidin, V. K. Verselis, M. V. Bennett, T. A. Bargiello, Functional alterations in gap junction channels formed by mutant forms of connexin 32: Evidence for loss of function as a pathogenic mechanism in the X-linked form of Charcot-Marie-Tooth disease. *Brain Res.* **900**, 9–25 (2001).
42. P. E. Martin, E. T. Mambetisaeva, D. A. Archer, C. H. George, W. H. Evans, Analysis of gap junction assembly using mutant connexins detected in Charcot-Marie-Tooth X-linked disease. *J. Neurochem.* **74**, 711–720 (2000).
43. C. Resso, D. Gomes, A. Dautigny, D. Pham-Dinh, R. Bruzzone, Connexin32 mutations associated with X-linked Charcot-Marie-Tooth disease show two distinct behaviors: Loss of function and altered gating properties. *J. Neurosci.* **18**, 4063–4075 (1998).
44. T. M. Suchyna, J. M. Nitsche, M. Chilton, A. L. Harris, R. D. Veenstra, B. J. Nicholson, Different ionic selectivities for connexins 26 and 32 produce rectifying gap junction channels. *Biophys. J.* **77**, 2968–2987 (1999).
45. V. H. Hernandez, M. Bortolozzi, V. Pertegato, M. Beltramello, M. Giarin, M. Zaccolo, S. Pantano, F. Mammano, Unitary permeability of gap junction channels to second messengers measured by FRET microscopy. *Nat. Methods* **4**, 353–358 (2007).
46. G. Kanaporis, P. R. Brink, V. Valiunas, Gap junction permeability: Selectivity for anionic and cationic probes. *Am. J. Physiol. Cell Physiol.* **300**, C600–C609 (2011).
47. D. Patel, X. Zhang, R. D. Veenstra, Connexin hemichannel and pannexin channel electrophysiology: How do they differ? *FEBS Lett.* **588**, 1372–1378 (2014).
48. A. Butterweck, U. Gergs, C. Elfgang, K. Willecke, O. Traub, Immunohistochemical characterization of the gap junction protein connexin45 in mouse kidney and transfected human HeLa cells. *J. Membr. Biol.* **141**, 247–256 (1994).
49. R. D. Veenstra, Voltage clamp limitations of dual whole-cell gap junction current and voltage recordings. I. Conductance measurements. *Biophys. J.* **80**, 2231–2247 (2001).
50. S. Oh, C. K. Abrams, V. K. Verselis, T. A. Bargiello, Stoichiometry of transjunctional voltage-gating polarity reversal by a negative charge substitution in the amino terminus of a connexin32 chimera. *J. Gen. Physiol.* **116**, 13–32 (2000).
51. A. Oshima, Structure and closure of connexin gap junction channels. *FEBS Lett.* **588**, 1230–1237 (2014).
52. E. De Vuyst, E. Deckrock, L. Cabooter, G. R. Dubyak, C. C. Naus, W. H. Evans, L. Leybert, Intracellular calcium changes trigger connexin 32 hemichannel opening. *EMBO J.* **25**, 34–44 (2006).
53. C. Peracchia, Chemical gating of gap junction channels. *Biochim. Biophys. Acta* **1662**, 61–80 (2004).
54. K. Torok, K. Stauffer, W. H. Evans, Connexin 32 of gap junctions contains two cytoplasmic calmodulin-binding domains. *Biochem. J.* **326**(Pt 2), 479–483 (1997).
55. L. Tao, A. L. Harris, 2-aminoethoxydiphenyl borate directly inhibits channels composed of connexin26 and/or connexin32. *Mol. Pharmacol.* **71**, 570–579 (2007).
56. D. Bai, C. del Corso, M. Srinivas, D. C. Spray, Block of specific gap junction channel subtypes by 2-aminoethoxydiphenyl borate (2-APB). *J. Pharmacol. Exp. Ther.* **319**, 1452–1458 (2006).
57. X. Guan, B. F. Cravatt, G. R. Ehring, J. E. Hall, D. L. Boger, R. A. Lerner, N. B. Gilula, The sleep-inducing lipid oleamide deconvolutes gap junction communication and calcium wave transmission in glial cells. *J. Cell Biol.* **139**, 1785–1792 (1997).
58. L. Venance, D. Piomelli, J. Glowinski, C. Giaume, Inhibition by anandamide of gap junctions and intercellular calcium signalling in striatal astrocytes. *Nature* **376**, 590–594 (1995).
59. F. F. Bukauskas, K. Jordan, A. Bukauskiene, M. V. L. Bennett, P. D. Lampe, D. W. Laird, V. K. Verselis, Clustering of connexin 43-enhanced green fluorescent protein gap junction channels and functional coupling in living cells. *Proc. Natl. Acad. Sci. U.S.A.* **97**, 2556–2561 (2000).
60. S. Oh, Y. Ri, M. V. L. Bennett, E. B. Trexler, V. K. Verselis, T. A. Bargiello, Changes in permeability caused by connexin 32 mutations underlie X-linked Charcot-Marie-Tooth disease. *Neuron* **19**, 927–938 (1997).
61. M. H. Kubala, O. Kovtun, K. Alexandrov, B. M. Collins, Structural and thermodynamic analysis of the GFP:GFP-nanobody complex. *Protein Sci.* **19**, 2389–2401 (2010).
62. S. Q. Zheng, E. Palovcak, J. P. Armache, K. A. Verba, Y. Cheng, D. A. Agard, MotionCor2: Anisotropic correction of beam-induced motion for improved cryo-electron microscopy. *Nat. Methods* **14**, 331–332 (2017).
63. K. Zhang, Gctf: Real-time CTF determination and correction. *J. Struct. Biol.* **193**, 1–12 (2016).
64. S. H. Scheres, RELION: Implementation of a Bayesian approach to cryo-EM structure determination. *J. Struct. Biol.* **180**, 519–530 (2012).
65. J. Zivanov, T. Nakane, B. O. Forsberg, D. Kimanius, W. J. H. Hagen, E. Lindahl, S. H. W. Scheres, New tools for automated high-resolution cryo-EM structure determination in RELION-3. *eLife* **7**, e42166 (2018).
66. A. Punjani, J. L. Rubinstein, D. J. Fleet, M. A. Brubaker, cryoSPARC: Algorithms for rapid unsupervised cryo-EM structure determination. *Nat. Methods* **14**, 290–296 (2017).
67. A. Kucukelbir, F. J. Sigworth, H. D. Tagare, Quantifying the local resolution of cryo-EM density maps. *Nat. Methods* **11**, 63–65 (2014).
68. E. F. Pettersen, T. D. Goddard, C. C. Huang, G. S. Couch, D. M. Greenblatt, E. C. Meng, T. E. Ferrin, UCSF Chimera—A visualization system for exploratory research and analysis. *J. Comput. Chem.* **25**, 1605–1612 (2004).
69. P. Emsley, B. Lohkamp, W. G. Scott, K. Cowtan, Features and development of Coot. *Acta Crystallogr. D Biol. Crystallogr.* **66**, 486–501 (2010).
70. P. D. Adams, P. V. Afonine, G. Bunkóczi, V. B. Chen, I. W. Davis, N. Echols, J. J. Headd, L. W. Hung, G. J. Kapral, R. W. Grosse-Kunstleve, A. J. McCoy, N. W. Moriarty, R. Oeffner, R. J. Read, D. C. Richardson, J. S. Richardson, T. C. Terwilliger, P. H. Zwart, PHENIX: A comprehensive Python-based system for macromolecular structure solution. *Acta Crystallogr. D Biol. Crystallogr.* **66**, 213–221 (2010).
71. C. Qi, S. Sorrentino, O. Medalia, V. M. Korkhov, The structure of a membrane adenyllyl cyclase bound to an activated stimulatory G protein. *Science* **364**, 389–394 (2019).
72. V. B. Chen, W. B. Arendall III, J. J. Headd, D. A. Keedy, R. M. Immormino, G. J. Kapral, L. W. Murray, J. S. Richardson, D. C. Richardson, MolProbity: All-atom structure validation for macromolecular crystallography. *Acta Crystallogr. D Biol. Crystallogr.* **66**, 12–21 (2010).
73. The PyMOL Molecular Graphics System, version 2.0, Schrödinger LLC.

74. E. F. Pettersen, T. D. Goddard, C. C. Huang, E. C. Meng, G. S. Couch, T. I. Croll, J. H. Morris, T. E. Ferrin, UCSF ChimeraX: Structure visualization for researchers, educators, and developers. *Protein Sci.* **30**, 70–82 (2021).
75. C. UniProt, UniProt: The universal protein knowledgebase in 2021. *Nucleic Acids Res.* **49**, D480–D489 (2021).
76. J. Cox, M. Mann, MaxQuant enables high peptide identification rates, individualized p.p.b.-range mass accuracies and proteome-wide protein quantification. *Nat. Biotechnol.* **26**, 1367–1372 (2008).
77. H. Wickham, M. Averick, J. Bryan, W. Chang, L. McGowan, R. François, G. Golemund, A. Hayes, L. Henry, J. Hester, M. Kuhn, T. Pedersen, E. Miller, S. Bache, K. Müller, J. Ooms, D. Robinson, D. Seidel, V. Spinu, K. Takahashi, D. Vaughan, C. Wilke, K. Woo, H. Yutani, Welcome to the Tidyverse. *J. Open Source Software* **4**, 1686 (2019).
78. J.-P. Quast, D. Schuster, P. Picotti, C. Arighi, pratti: An R package for comprehensive data analysis of peptide- and protein-centric bottom-up proteomics data. *Bioinform. Adv.* **2**, vbab041 (2022).
79. Y. Perez-Riverol, J. Bai, C. Bandla, D. Garcia-Seisdedos, S. Hewapathirana, S. Kamatchinathan, D. J. Kundu, A. Prakash, A. Frericks-Zipper, M. Eisenacher, M. Walzer, S. Wang, A. Brazma, J. A. Vizcaino, The PRIDE database resources in 2022: A hub for mass spectrometry-based proteomics evidences. *Nucleic Acids Res.* **50**, D543–D552 (2022).
80. K. Alboukadel, ggpubr: 'ggplot2' based publication ready plots, R package version 0.4.0 (2020).
81. G. Koulouras, A. Panagopoulos, M. A. Rapsomaniki, N. N. Giakoumakis, S. Taraviras, Z. Lygerou, EasyFRAP-web: A web-based tool for the analysis of fluorescence recovery after photobleaching data. *Nucleic Acids Res.* **46**, W467–W472 (2018).

Acknowledgments: We thank E. Poghosian (EM Facility, Paul Scherrer Institute) and M. Peterek (ScopeM, ETH Zurich) for expert support in cryo-EM data collection. We also thank S. Bliven and M. Caubet-Serrabou (Paul Scherrer Institute) for the support in high-performance computing. We also thank D. Penton Ribas (Electrophysiology Facility, University of Zurich) for expert support in electrophysiology. **Funding:** The work was supported by a grant from Horten Foundation (grant to V.M.K.), the Swiss National Science Foundation (grant 184951 to V.M.K.), and the AFM Telethon (grant 23333 to M.B.). **Author contributions:** Conceptualization: M.B. and V.M.K. Methodology: C.Q., P.L., E.B., A.V., D.S., M.B., and V.M.K. Investigation: C.Q., P.L., E.B., A.V., D.S., M.P., V.S., M.B., and V.M.K. Visualization: C.Q., P.L., E.B., A.V., D.S., M.B., and V.M.K. Funding acquisition: M.B. and V.M.K. Project administration: M.B. and V.M.K. Supervision: P.P., M.B., and V.M.K. Writing—original draft: C.Q., P.L., E.B., M.B., and V.M.K. Writing—review and editing: C.Q., P.L., E.B., A.V., D.S., M.P., V.S., P.P., M.B., and V.M.K. **Competing interests:** The authors declare that they have no competing interests. **Data and materials availability:** The coordinates and the cryo-EM density map have been deposited to PDB and Electron Microscopy Data Bank with the following accession numbers: PDB ID 7ZXM, EMD-15010; PDB ID 7ZXN, EMD-15011; PDB ID 7ZXO, EMD-15012; PDB ID 7ZXP, EMD-15013; PDB ID 7ZXQ, EMD-15014; and PDB ID 7ZXT, EMD-15016. The MS data have been deposited to the ProteomeXchange Consortium via the PRIDE partner repository with the dataset identifiers PXD039379, PXD033848, and PXD033671. The code for HC assay analysis software has been deposited in Zenodo (8185751). All data needed to evaluate the conclusions in the paper are present in the paper and/or the Supplementary Materials.

Submitted 7 March 2023

Accepted 27 July 2023

Published 30 August 2023

10.1126/sciadv.adh4890

Structures of wild-type and selected CMT1X mutant connexin 32 gap junction channels and hemichannels

Chao Qi, Pia Lavriha, Erva Bayraktar, Anand Vaithia, Dina Schuster, Micaela Pannella, Valentina Sala, Paola Picotti, Mario Bortolozzi, and Volodymyr M. Korkhov

Sci. Adv., **9** (35), eadh4890.
DOI: 10.1126/sciadv.adh4890

View the article online

<https://www.science.org/doi/10.1126/sciadv.adh4890>

Permissions

<https://www.science.org/help/reprints-and-permissions>

Use of this article is subject to the [Terms of service](#)

Science Advances (ISSN) is published by the American Association for the Advancement of Science. 1200 New York Avenue NW, Washington, DC 20005. The title *Science Advances* is a registered trademark of AAAS.
Copyright © 2023 The Authors, some rights reserved; exclusive licensee American Association for the Advancement of Science. No claim to original U.S. Government Works. Distributed under a Creative Commons Attribution NonCommercial License 4.0 (CC BY-NC).